applied sciences

MDPI

Article

Fast-Scale Instability and Stabilization by Adaptive Slope Compensation of a PV-Fed Differential Boost Inverter

Abdelali El Aroudi [1,*,†], Mohamed Debbat [2,†], Mohammed Al-Numay [3,†] and Abdelmajid Abouloiafa [4,†]

[1] Department of Electronics, Electrical Engineering and Automatic Control, Universitat Rovira i Virgili, 43002 Tarragona, Spain
[2] Department of Electrical Engineering, University Mustapha Stambouli of Mascara, Mascara 29000, Algeria; mohamed.debbat@univ-mascara.dz
[3] Electrical Engineering Department, King Saud University, Riyadh 11451, Saudi Arabia; alnumay@ksu.edu.sa
[4] Electrical Engineering and Automatic Control, Hassan II University of Casablanca, Casablanca 20000, Morocco; abdelmajid.abouloifa@univh2c.ma
* Correspondence: abdelali.elaroudi@urv.cat; Tel.: +34-977558522
† These authors contributed equally to this work.

Abstract: Numerical simulations reveal that a single-stage differential boost AC module supplied from a PV module under an Maximum Power Point Tracking (MPPT) control at the input DC port and with current synchronization at the AC grid port might exhibit bifurcation phenomena under some weather conditions leading to subharmonic oscillation at the fast-switching scale. This paper will use discrete-time approach to characterize such behavior and to identify the onset of fast-scale instability. Slope compensation is used in the inner current loop to improve the stability of the system. The compensation slope values needed to guarantee stability for the full range of operating duty cycle and leading to an optimal deadbeat response are determined. The validity of the followed procedures is finally validated by a numerical simulations performed on a detailed circuit-level switched model of the AC module.

Keywords: DC-AC inverters; fast-scale instability; slope compensation; three-loop current mode control; AC module; boost inverter; microinverter

Citation: El Aroudi, A.; Debbat, F.M.; Al-Numay, M.; Abouloiafa, A. Fast-Scale Instability and Stabilization by Adaptive Slope Compensation of a PV-Fed Differential Boost Inverter. *Appl. Sci.* **2021**, *11*, 2106. https://doi.org/10.3390/app11052106

Academic Editor: Roman Starosta

Received: 1 January 2021
Accepted: 18 February 2021
Published: 27 February 2021

1. Introduction

The demand for small-scale renewable energy systems is increasingly growing [1–4]. DC-AC inverters are essential elements for these systems [4]. They are used for efficient energy conversion either to supply local AC loads or to inject part of the electrical power into the AC grid [3].

In conventional PV systems, the PV arrays are formed using multiple series-connected PV modules to attain high enough DC voltage at the PV side. The resulting arrays are then arranged in parallel according to the needed power to be generated [4]. With this approach the partial shadowing of some of the PV modules in the arrays causes the operating point of shaded modules to be different from the rest of modules and therefore the total generated power is significantly decreased [2,4]. Furthermore, a high irradiance mismatch between PV sources may lead to damaging over-voltages in the modules [2,4]. To mitigate this problem, the AC module approach (known in the literature as micro inverter approach) has been proposed [3,4]. With this approach, a small DC-AC inverter is used for each individual PV module. PV systems based on AC module approach has many advantages over central and string inverter systems and it is foreseen to be the future trend of PV system architectures. These advantages include small size, good quality of supplied electrical power, high conversion efficiency, good reliability, robust stability, simple and flexible installation options and enhanced safety.

There exist mainly two kinds of architectures for integrating AC modules into a power generation system. The first one uses a single-stage inverter with a step-up transformer [3].

The unique stage is in charge for regulating the DC PV voltage, performing Maximum Power Point Tracking (MPPT) and carrying out DC-AC conversion. The second one is based on a double-stage approach where the first stage is a front-end DC-DC converter used to sufficiently stepping-up the DC voltage at the PV side while performing MPPT and the second stage is a DC-AC inverter used in to generate AC voltage [3,4]. Both topologies suffer from decreased efficiency and increased size.

Single-stage transformer-less DC-AC boost inverters have recently received a considerable attention from many researchers, see [3] and references therein. These structures apart from performing DC-AC conversion they also step-up the voltage being therefore excellent candidates for microinverter applications. The price of single-stage inverter topologies is also low, and their size is reduced because of using small reactive components. Furthermore, their efficiency is better [5].

The differential boost inverter has been introduced in [6] and since then many studies have dealt with its control design [6–10]. In most of the studies, inverters with a constant input voltage and an ohmic resistance as a load have been considered and their control design has been accordingly tackled. In [7,10,11], a grid-connected boost inverter has been considered and its control design has been addressed.

Like many other practical engineering systems whose dynamics are governed by switching among different circuit topologies, power conversion systems can be classified into to the category of nonlinear piecewise smooth systems [12]. The main research works on the nonlinear dynamics of this kind of systems have hitherto dealt with the behavior of simple DC-DC converters with linear and mostly resistive loads [13–18] due to the relative simplicity of their models. The nonlinear modeling of pulse width modulated DC-DC converters is relatively simple in the sense that their behavior is governed by a single constant switching frequency. In contrast, the dynamics of AC-DC rectifiers and DC-AC inverters are governed by two vastly distant frequencies: the switching high frequency f_s and the grid low frequency f_g [19–25]. Their nonlinear modeling is therefore mathematically more involved. However, if the ratio $m = f_s/f_g$, known as the *modulation ratio*, is enough high which is the case in many applications, *quasi-static approximation* can be used. Specifically, when the system dynamics at the switching scale are sufficiently fast, then the quasi-static approximation leads to enough accurate expressions for predicting fast-scale instability in AC-DC rectifiers [25] and in DC-AC inverters [26]. This approximation is a commonly used technique for analyzing DC-AC inverters [26,27] and AC-DC rectifiers [25,27].

This kind of systems is also featured with multi-time scale operation and their dynamical behavior has received and still receiving a great attention from researchers all over the world. The fast-scale operation in DC-AC inverters is usually averaged and the switching details have been conventionally overlooked. Although some past works dealing with nonlinear dynamical behavior of DC-AC inverters exist, the PV-fed grid-tied DC-AC boost inverter for AC module applications has not been studied from the perspective of nonlinear dynamics and its slope compensation has not been addressed. Fast-scale instability in such AC modules can cause the power generation system to be subject to faults or unfavorable conditions and the system reliability may be degraded which can negatively impacts the system performance. This is because fast-scale instability could increase the ripples of the electrical variables which results in higher overall losses and current stress on the switching devices. The power quality can also be compromised by this fast-scale instability since it can increase the Total Harmonic Distortion (THD). That being the case, accurate modeling of the dynamical behavior of the modules and their fast-scale stability analysis are needed. To have a reliable functioning, the instability must be avoided for the full range of system parameter values. For that, the right compensating must be used.

In general, it can be claimed that the methods of analysis and modeling applied to power electronics systems are based, to a large extent, on the averaging approach. DC-DC converters have been also studied by using accurate discrete-time approaches. However, to date little has been done to study the qualitative dynamical aspects of DC-AC

inverters based on accurate modeling and analysis approaches. The aim of this study is to faithfully determine the outbreak of fast-scale instability in a grid-tied differential boost AC module by combining numerical and analytical procedures and to obtain the required compensation ramp signal slope ensuring stability of the module for the full range of the operating duty cycle.

The rest of this paper is structured as follows. In Section 2, the PV-fed DC-AC grid-tied AC module under a three-loop differential Current Mode Control (CMC) is briefly described. In Section 3, the dynamics of the AC module is explored disclosing that its behavior depends on parameters of different nature but all affecting the operating quasi-static operating duty cycle. In particular, the AC module is shown to manifest fast-scale instability over specific intervals within the grid period causing bubbling phenomenon in some of the state variables waveforms. Thereafter, in Section 4, approximate analysis and prediction of fast-scale instability is preformed obtaining the required compensating slope for achieving stability for all operating duty cycle values and for an optimum fast-scale *deadbeat* response of the AC module using an adaptive compensation scheme. Finally, in Section 5 the concluding remarks of this study are outlined.

2. Differential Boost AC Module Under Three-Loop Control

The system studied in this paper is a grid-tied differential boost inverter supplied by a PV generator for AC module applications. The circuit schematic diagram of its power stage and the block diagram of its controller are shown in Figure 1. The system is under a differential CMC strategy to decide the state of its four switches. Specifically, its strategy is based on three control loops: a first loop which oversees regulating the DC PV voltage to the value provided by the MPPT controller, a second loop synchronizes the grid current to the grid voltage and a third differential peak CMC loop for limiting the peak value of the difference between its inductor currents. Specifically, a comparator is used to compare the signal $R_s(i_1 - i_2) + v_r$ with the signal $R_s i_{\text{ref}}$, where v_r is an artificial ramp signal with slope $m_r = V_M/T$, V_M being its amplitude and T its period. The output of the comparator is connected to the RESET pin of a flip-flop and a periodic clock signal is connected to its SET input. The Q and $\overline{\text{Q}}$ outputs of the flip-flop are the driving pulses for the switches Q_1–Q_4 as shown in Figure 1. A type-III controller was demonstrated to be effective for controlling the grid current in the system [10]. Its transfer function in the Laplace s—domain can be expressed as follows [28]:

$$H_c(s) = \kappa_{\text{pc}} \frac{\omega_z}{s} \frac{(s/\omega_z + 1)^2}{(s/\omega_p + 1)^2}. \tag{1}$$

where κ_{pc} is a suitable proportional gain of the controller, ω_z is its double zero and ω_p is its double pole. The placement of the poles and zeros can be performed according to the rules explained in [28]. The signal $R_s i_{\text{ref}}$ for the current difference $R_s(i_1 - i_2)$ is the output of the type-III controller which is responsible for making the grid current i_g to track its reference $R_{sg} i_{\text{gref}}$. For active power control, this reference signal is made proportional to the grid voltage $v_g = V_g\sqrt{2}\sin(\omega_g t)$, $\omega_g = 2\pi f_g$. This is achieved by means of a Phase-Locked Loop (PLL) which generates a sinusoidal signal $\sin(\omega_g t)$ in phase with the grid voltage. The signal obtained by multiplying the output of the PLL and the output of the PV voltage controller gives the time varying reference $R_{sg} i_{\text{gref}}$ that can be expressed as follows

$$R_{sg} i_{\text{gref}} = R_{sg} I_{\text{gref}} \sin(\omega_g t) \tag{2}$$

The PV voltage v_{dc} is regulated by a simple PI controller that aims to make it equal on average to the reference voltage V_{mpp}. This reference voltage is decided by an MPPT controller. To reduce the harmonic content in the feedback loop, a low-pass filter is also placed after the PV voltage sensor. Therefore, the controller processes the error voltage $v_f - V_{\text{mpp}}$, where v_f is the filtered PV voltage. The cut-off frequency ω_c of the filter is

selected at the grid frequency w_g. The resulting s—domain v_{dc}-to-$R_{sg}I_{\mathrm{gref}}$ transfer function can be accordingly written in the following form

$$H_v(s) = \frac{\kappa_{\mathrm{pv}}}{\tau s}\frac{(1+\tau s)}{(1+s/\omega_c)}. \tag{3}$$

where κ_{pv} is a suitable proportional gain of the controller and τ is its time constant. Therefore, the amplitude $R_s I_{\mathrm{gref}}$ of the grid current reference signal $R_{sg}i_{\mathrm{gref}}$ can be expressed as follows

$$R_s I_{\mathrm{gref}} = \kappa_{\mathrm{pv}}(v_f - V_{\mathrm{mpp}} + \frac{v_{i2}}{\tau}) \tag{4}$$

where the variable $v_{i2} = \int (v_f - V_{\mathrm{mpp}})\mathrm{d}t$ is the integral of the error signal $v_f - V_{\mathrm{mpp}}$. Therefore (2) becomes as follows

$$R_{sg}i_{\mathrm{gref}} = \kappa_{\mathrm{pv}}(v_f - V_{\mathrm{mpp}} + \frac{v_{i2}}{\tau})\sin(\omega_g t) \tag{5}$$

The MPPT inputs are the PV current i_{pv} and the PV voltage v_{dc}. From these inputs the PV power p_{pv} is obtained and sampled at a constant frequency rate $f_{\mathrm{mppt}} = 1/T_{\mathrm{mppt}}$.

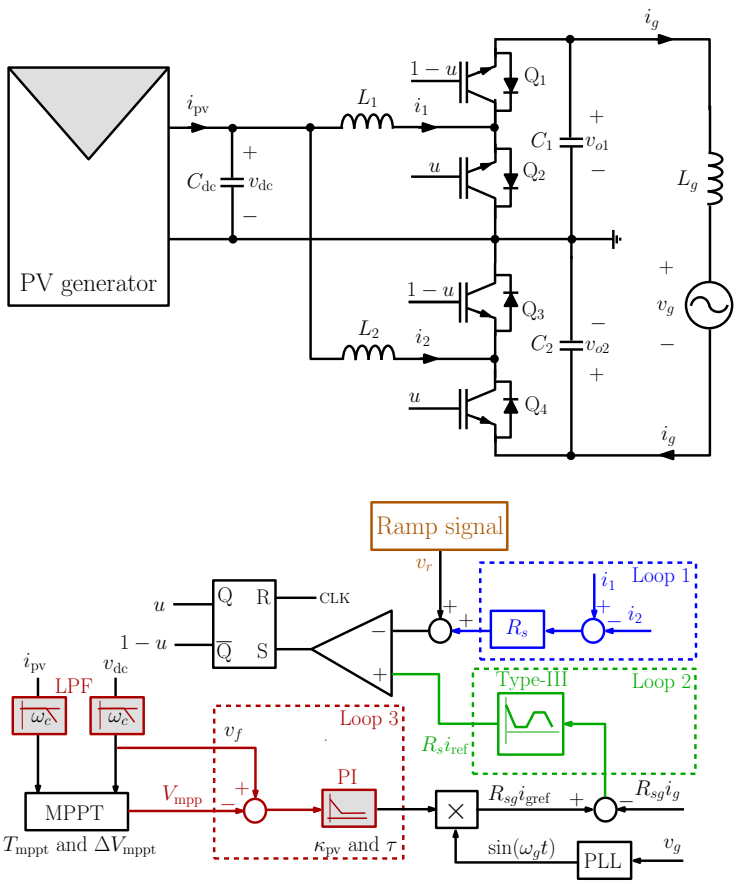

Figure 1. Single-stage grid-tied PV-fed differential boost AC module.

3. Nonlinear Behavior and Fast-Scale Instability in the Differential Boost Inverter

For the purpose of gaining insight on appropriate ways of obtaining an accurate mathematical model that can be used for accurately performing stability analysis, the system dynamical behavior is explored here by using numerical simulations performed on the switched model of the inverter implemented in PSIM© software [29]. The simulations have been performed using the parameter values for the inverter power stage shown in Table 1 and the values of the control parameters shown in Table 2. The PV source used

consists of a string of four series-attached modules. The parameter values of one module are specified in [30] and outlined in Table 3.

The focus here is on fast-scale system stability as affected by time varying sinusoidal voltage reference under different weather conditions. For that, only steady-state operation of the closed-loop system will be shown. A fixed value of temperature ($\Theta = 25\ ^{\circ}\mathrm{C}$) was used while changing the irradiance. The output of the PV-fed differential boost AC module is tied to a 230 V AC, 50 Hz grid voltage performing active power control as described previously. The MPPT is performed using a conventional Perturb and Observe (P&O) algorithm providing the voltage reference V_{mpp} for the average value of the DC PV voltage v_{dc}. The MPPT controller uses a sampling period $T_{\mathrm{mppt}} = 0.2$ s equal to 10 times the PV voltage loop settling time which was designed to be equal to one grid cycle ($t_s = 0.02$ ms). The perturbation amplitude applied to V_{mpp} is $\Delta V_{\mathrm{mpp}} = 5$ V. The irradiance S was varied between two different levels representing a sunny and a cloudy day. The time-domain response was obtained, and only steady-state behavior is represented. All the variables are sampled at the switching frequency rate to have a clear picture of the system steady-state behavior. Sampling the state variables helps in clearly illustrating the bubbling phenomenon.

Table 1. Parameter values for the power stage circuit.

Parameter	Value
$L_1 = L_2 = L$ and L_g	100 µH and 5 mH
$C_1 = C_2 = C$	22 µF
C_{dc}	2 mF
f_s	50 kHz
f_g	50 Hz
V_g	$230\sqrt{2}$ V

Table 2. Parameter values of the controllers.

Parameter	Value
R_s and R_{sg}	0.1 Ω and 1 Ω
τ	0.0247 s
κ_{pv}	0.2
$\omega_c/(2\pi)$	50 Hz
$\omega_z/(2\pi)$ and $\omega_p/(2\pi)$	500 Hz and 50 kHz
κ_{pc}	2

Table 3. The used parameter values for one single module.

Parameter	Value
Number of series-connected cells in a module	72
Open-circuit voltage V_{oc}	46.5 V
Short-circuit current I_{sc}	9.60 A
Maximum power voltage V_{mpp}	38.4 V
Maximum power current I_{mpp}	9.13 A

3.1. Test 1: $S = 1000\ W/m^2$ and $\Theta = 25\ ^\circ C$

Figure 2 shows the waveforms of the extracted power p_{pv} from the PV source and the maximum available power P_{max} in the PV generator, the PV voltage v_{dc} and its reference V_{mpp} provided by the MPPT controller for irradiance level S =1000 W/m^2 ($P_{\text{max}} \approx 1.4$ kW). It can be noticed that the reference signal V_{mpp} dictated by the MPPT algorithm oscillates among three levels according to the values of the MPPT sampling period $T_{\text{mppt}} = 0.2$ s and the perturbation amplitude $\Delta V_{\text{mpp}} = 5$ V. Notice also that the average of the PV voltage is regulated to the MPP voltage V_{mpp} with the specified settling time and that the extracted power is equal to the maximum available one. The inductor currents i_1 and i_2 and the capacitor voltages v_{o1} and v_{o2} for the same irradiance value are depicted in Figure 3. Notice how the voltages v_{o1} and v_{o2} are out of phase and their difference $v_{o1} - v_{o2}$ is the grid voltage v_g. Notice also how with irradiance level S =1000 W/m^2, the sampled state variables evolve as expected and the system is free from any kind of instability and undesired nonlinear behavior.

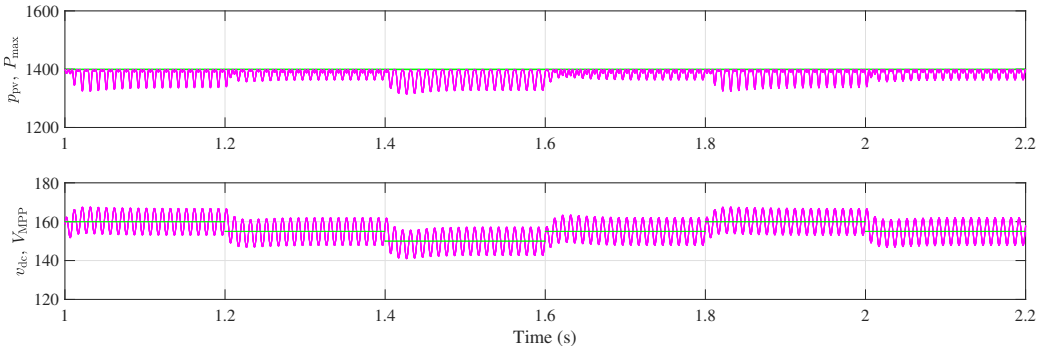

Figure 2. Time-domain waveforms of the sampled extracted power p_{pv} for $S = 1000$ W/m^2 in steady-state operation. $V_M = 3.2$ V.

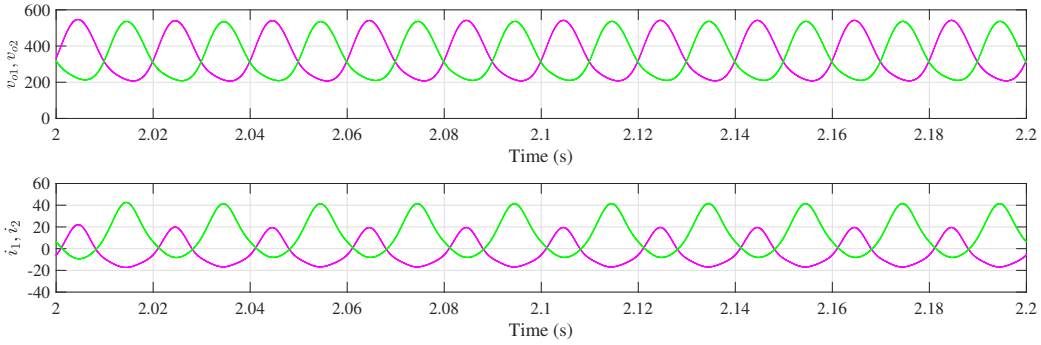

Figure 3. The sampled inductor currents $i_1(nT)$ and $i_2(nT)$ and capacitor voltages $v_{o1}(nT)$ and $v_{o2}(nT)$ for $S = 1000$ W/m^2 in steady-state operation. $V_M = 3.2$ V.

Figure 4 shows the grid voltage v_g and the injected grid current i_g. The plot shows that these grid variables are in phase and their THD is low. In particular, for $S = 1000$ W/m^2 ($P_{\text{max}} \approx 1.4$ kW), the THD of i_g is about 1% as calculated by PSIM© software.

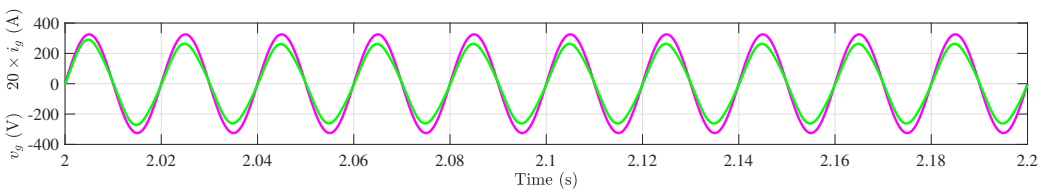

Figure 4. Time-domain waveforms of the sampled grid voltage v_g and sampled grid current i_g for $S = 1000$ W/m^2 in steady-state operation. $V_M = 3.2$ V.

3.2. Test 2: $S = 200\ W/m^2$ and $\Theta = 25\ ^\circ C$

The previous simulation was repeated for a lower value of irradiance representing a cloudy day or during the startup of the system in the early morning.

Figure 5 shows the waveforms of the extracted power p_{pv}, the maximum available power P_{max} and the PV voltage v_{dc} and its reference V_{mpp} provided by the MPPT controller for S =200 W/m^2 ($P_{\text{max}} \approx 250$ W). As before, the reference signal V_{mpp} oscillates among three levels. The average of the PV voltage is regulated to the MPP voltage V_{mpp} and the extracted power from the PV source is also close to the maximum available power.

However, by examining the waveforms of the sampled inductor currents (Figure 6), fast-scale instability can be clearly observed. This instability is barely noticed in the capacitor voltages v_{o1} and v_{o2} for the used values of parameters as can be observed in the top panel of Figure 6. Notice how the dynamic behavior of the closed-loop system is similar to the previous case at the slow scale. However, the fast-scale dynamics is unstable. Indeed, bubbling of the sampled waveforms take place during specific intervals within the grid cycle. This bubbling phenomenon is manifested as period doubling bifurcation first and then as a period halving as time increases within a grid cycle. The process repeats each cycle.

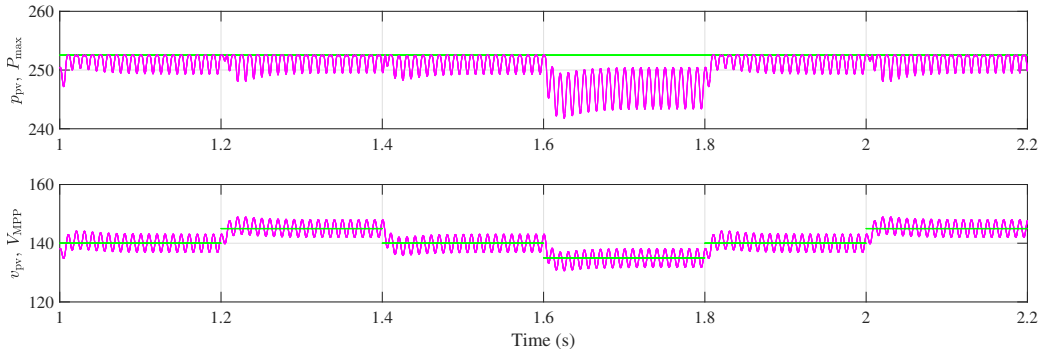

Figure 5. Time-domain waveforms of the sampled extracted power p_{pv} for $S = 200$ W/m^2 in steady-state operation. $V_M = 3.2$ V.

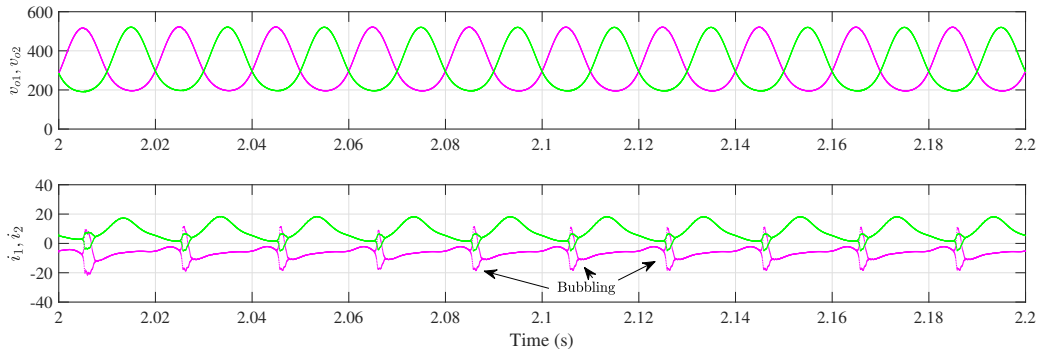

Figure 6. The sampled inductor currents $i_1(nT)$ and $i_2(nT)$ and capacitor voltages $v_{o1}(nT)$ and $v_{o2}(nT)$ for $S = 200$ W/m^2 in steady-state operation. $V_M = 3.2$ V.

Figure 7 shows the grid voltage v_g and the injected grid current i_g for $S = 200$ W/m^2 ($P_{\text{max}} \approx 250$ W). One can observe that v_g and i_g are still in phase as before. However, for this value of irradiance, the THD value of the grid current i_g is larger (about 2%) and it could be even higher if other parameters are changed such that the bubbling phenomenon occupies larger intervals within the grid cycle.

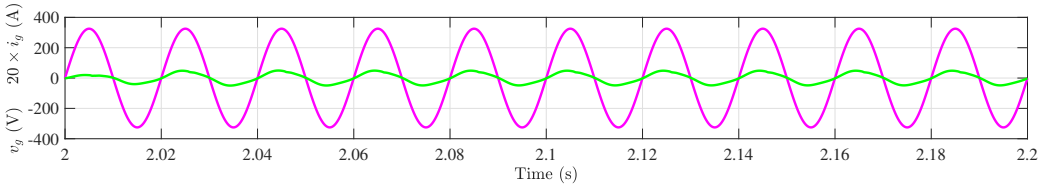

Figure 7. Time-domain waveforms of the grid voltage v_g and grid current i_g for $S = 200$ W/m^2 in steady-state operation. $V_M = 3.2$ V.

4. Approximate Prediction of Fast-Scale Instability and Adaptive Slope Compensation

The model of a DC-AC boost inverter including its control loop is high-dimensional which makes its accurate stability analysis a real challenge at both the fast and the slow scales. Although the exact full-order switched model or the associated discrete-time model [31,32] can be used to numerically predict and explain any king of instability that could take place in the system, it is more useful to have a simple and design-oriented expression clearly putting in evidence the impact of all the relevant system parameters affecting the stability of the system [33]. If fast-scale instability is of concern, the conventional averaged model will fail to predict this behavior because its validity is limited to frequency ranges much below the switching frequency since the switching effects are naturally eliminated by the averaging process. Fast-scale instability is a high frequency behavior requiring a model that takes into account the switching action and its related sampling effects [34]. The accuracy of the averaged model can be improved by taking into account these sampling effect. In this way, the fast-scale instability can be predicted using the frequency response of the system loop gain. However, as stated before, it is more useful to have explicit mathematical expressions that predict this behavior to appropriately select the system parameter values guaranteeing a stable behavior. A simple reduced-order discrete-time model will be enough to approximately but accurately predict the onset of this phenomenon [27]. Specifically, fast-scale instability is dominated by the fast inner current loop and its parameters although the slow outer loop parameters could appear, under some realistic conditions, in a negligible correcting term. Therefore, a reduced-order model taking into account only the main variables used in the fast current loop can be used to predict fast-scale instability and to obtain a simple design-oriented expression for selecting the right slope ensuring stability for all operating range of the duty cycle. This model will be presented below and then used to perform stability analysis at the fast scale.

4.1. Reduced-Order Discrete-Time Model for Predicting the Fast-Scale Instability in the DC-AC Inverter

For the DC-AC boost inverter considered in this study, the current loop is established by the signal $\sigma(t) = R_s(i_1(t) - i_2(t))$. A reduced-order discrete-time model that takes into account only this signal can be therefore used to mathematically predict the stability boundary. Therefore, let the discrete-time variable $\sigma_n = \sigma(nT) = R_s(i_1(nT) - i_2(nT))$. The approach followed here for analyzing the dynamics at the fast scale of the AC module is based on decoupling the different system loops into three subsystems. Indeed, since the switching frequency is much higher than the grid frequency ($m := f_s/f_g = 1000$), the quasi-static approximation can be used to model the fast current loop dynamics and stability criteria can be obtained. Since the focus in this paper is on the fast-scale instability, the slower loops are considered stable and well described by their averaged models. Moreover, steady-state average quantities of the variables involved in these slow loops are used in the description of the fast dynamics of the variable σ. The fast current loop dynamics is solved in discrete time to catch the high frequency dynamics in this loop which is dominant in inducing the previously observed phenomena.

Under the quasi-static conditions, the behavior of the system is considered to repeat for all grid periods. Notice that this was the case with the simulations presented in the previous section. Therefore, the study of the fast-scale dynamics is performed within one single grid period. Let us write $\theta = \omega_g t$, $\theta \in (0, 2\pi)$. Therefore, the grid voltage can be

written in terms of the phase angle as $v_g(\theta) = \sqrt{2}V_g \sin(\theta)$. Thanks to the quasi-static approximation, the time dependence of the inverter model at the slow scale is eliminated and the dynamics at the fast scale is parametrized by the phase angle θ which is treated as a slowly varying parameter.

Under the quasi-static approximation, and neglecting the switching dynamics of the slow loop, the switched model of the inverter considering the signal σ the only state variable of the system can be expressed as follows

$$\frac{\mathrm{d}\sigma}{\mathrm{d}t} = \frac{R_s}{L}((v_{o1}(\theta) - v_{o2}(\theta))u - v_{o1}(\theta)) \tag{6}$$

where $u \in \{0, 1\}$ is the binary switched signal representing the states of the switches Q_1–Q_4. The illustrative waveforms of the signals σ and $R_s i_{\mathrm{ref}}(\theta) - v_r$ are depicted in Figure 8. From this figure and by integrating (6) within a switching cycle, the discrete-time dynamics corresponding to the variable σ can be described by the following recurrence equation

$$\sigma_{n+1} = \sigma_n + m_1(\theta)d_n T + m_0(\theta)(1 - d_n)T \text{ with } 0 \leq d_n \leq 1. \tag{7}$$

where d_n is the duty cycle within the switching cycle $(nT, (n+1)T)$ for a phase angle $\theta \in (0, 2\pi)$. According to (6), the phase-dependent raising slope $m_1(\theta)$ $(u = 1)$ and the falling slope $m_0(\theta)$ $(u = 0)$ of the signal σ are given by

$$m_1(\theta) = R_s \frac{v_{o2}(\theta)}{L} \tag{8}$$

$$m_0(\theta) = -R_s \frac{v_{o1}(\theta)}{L} \tag{9}$$

where $v_{o1}(\theta)$ and $v_{o2}(\theta)$ can be expressed as follows [10,35]

$$v_{o1}(\theta) = \frac{V_{\mathrm{mpp}}}{1 - D(\theta)} \tag{10}$$

$$v_{o2}(\theta) = \frac{V_{\mathrm{mpp}}}{D(\theta)} \tag{11}$$

$D(\theta)$ is the time varying quasi-steady-state duty cycle that can be expressed as follows [10,35]:

$$D(\theta) = \frac{1}{2} - \frac{V_{\mathrm{mpp}}}{v_g(\theta)} + \mathrm{sign}(v_g(\theta))\frac{1}{2}\sqrt{1 + \frac{4V_{\mathrm{mpp}}^2}{v_g^2(\theta)}} \tag{12}$$

It is worth noting that $D(0^-) = D(0^+) = 1/2$ and therefore $D(\theta)$ is a continuous function of the phase angle θ. The quasi-steady-state duty cycle $D(\theta)$ is plotted in Figure 9 together with the duty cycle obtained from numerical simulations corresponding to the results presented in Figures 2–4 for $S = 1000\ \mathrm{W/m^2}$ and in Figures 5–7 for $S = 200\ \mathrm{W/m^2}$ respectively. Notice that the plots corresponding to the numerical simulations and the one obtained from the theoretical expression (12) cannot be distinguished from each other when the system operates in the expected behavior without fast-scale instability. Notice also that when the system exhibits instability, bubbling phenomenon mentioned previously also occurs in the waveforms of the quasi-steady-state duty cycle.

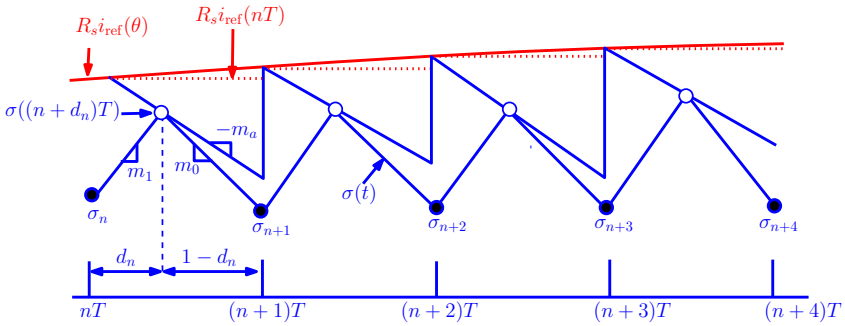

Figure 8. The feedback signal σ and the control signal $R_s\text{ref}(\theta) - v_r$.

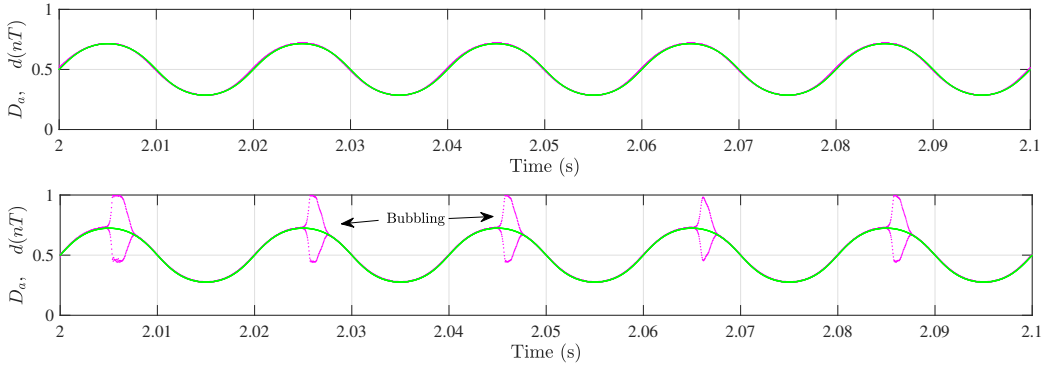

Figure 9. The time varying duty cycle calculated from (12) ($D(t)$) and obtained from numerical simulation ($d(nT)$, $n \in \mathbb{N}$) for $S = 1000$ W/m^2 and $S = 200$ W/m^2.

According to the switching decision corresponding to the control block diagram represented in Figure 1, the expression of the duty cycle d_n can be obtained by solving the following equation

$$R_s(i_1(d_nT) - i_2(d_nT)) + v_r(d_nT) - R_s i_{\text{ref}}(\theta) = 0 \tag{13}$$

By taking into account that $\sigma = R_s(i_1 - i_2)$, (13) becomes as follows

$$\sigma((n+d_n)T) = R_s i_{\text{ref}}(\theta) - v_r(d_nT) \tag{14}$$

Within the switching cycle $(nT, (n+1)T)$, $n \in \mathbb{N}$, and taking into account that $\sigma((n+d_n)T) = \sigma_n + m_1 d_n T =$ and $v_r(d_nT) = m_r d_n T$ (See Figure 8), (14) can be expressed as follows

$$\sigma_n + m_1 d_n T = R_s i_{\text{ref}}(\theta) - m_r d_n T \tag{15}$$

where, as stated previously, $m_r = V_M/T$ is the slope of the ramp signal v_r. The duty cycle d_n can be obtained by solving (15) while considering $R_s i_{\text{ref}}(\theta)$ constant within a switching cycle. Solving for d_n one gets

$$d_n = \frac{R_s i_{\text{ref}}(\theta) - \sigma_n}{(m_1(\theta) + m_r)T}. \tag{16}$$

The expressions (7) and (16) define the reduced-order model that can be used for performing the stability analysis of the DC-AC inverter at the fast-switching scale. Below this analysis will be performed and the stability criteria will be determined.

4.2. Fast-Scale Stability Analysis

The stability analysis at the fast scale can be performed by linearizing (7) together with (16) resulting in the following small-signal model

$$\hat{\sigma}_{n+1} \approx \lambda(\theta)\hat{\sigma}_n \tag{17}$$

where λ is the total derivative of σ_{n+1} with respect to σ_n that can be expressed as follows

$$\lambda(\theta) := \frac{\mathrm{d}\sigma_{n+1}}{\mathrm{d}\sigma_n} = \frac{\partial\sigma_{n+1}}{\partial\sigma_n} + \frac{\partial\sigma_{n+1}}{\partial d_n}\frac{\partial d_n}{\partial\sigma_n} = \frac{R_s m_0(\theta) + m_r}{R_s m_1(\theta) + m_r} \tag{18}$$

The solution of (17) starting from an initial condition σ_0 can be expressed as follows

$$\hat{\sigma}_n \approx \lambda^n(\theta)\hat{\sigma}_0 \tag{19}$$

Based on the previous equation, the current loop stability at the fast scale can be ensured if $|\lambda(\theta)| < 1$ since in this case a small initial disturbance will vanish as n increases. In quasi-steady-state operation one has that $\sigma_{n+1} \approx \sigma_n$, $d_n = D(\theta)$ and according to (7) one has $m_1 D(\theta) \approx -m_0(1 - D(\theta))$. Consequently, the expression of $\lambda(\theta)$ in (18) becomes as follows

$$\lambda(\theta) = \frac{R_s m_0(\theta) + m_r}{-\frac{R_s m_0(\theta)(1-D(\theta))}{D(\theta)} + m_r} \tag{20}$$

Expression (20) gives how the eigenvalue λ evolves when the phase angle varies in the full range $(0, 2\pi)$. However, for determining the boundary of the fast-scale instability, only the behavior of $\lambda(\theta)$ within the half range $(0, \pi)$ can be considered. Indeed, from Figure 9 it can be observed that the fast-scale instability emerges first within some switching cycles during the first half cycle of the sinewave signal eventually in the neighborhood to the quarter of the cycle where the signal $D(\theta)$ is maximum for $\theta \in (0, \pi)$ during which the quasi-static duty cycle $D \in (0.5, 1)$. Therefore, the analytical study that will be presented below will be restricted to this range of phase angle θ. The eigenvalue $\lambda(\theta)$ is plotted in Figure 10 in terms of the phase angle θ for different values of compensating signal amplitude V_M or equivalently its slope m_r. It can be observed that the eigenvalue $\lambda(\theta)$ has its minimum value at the phase angle $\pi/2$. If the minimum value of the eigenvalue is larger than -1 the system will not exhibit fast-scale instability. This is the case for instance for $V_M = 4$ V and for $V_M = 5$ V. On the other hand, for $V_M = 3$ V fast-scale instability will be exhibited for the phase angle $\theta \in (1.17, 1.96)$ rad because within this interval of θ one has $\lambda(\theta) < -1$. The limits of this interval are indicated by two dashed lines in Figure 10.

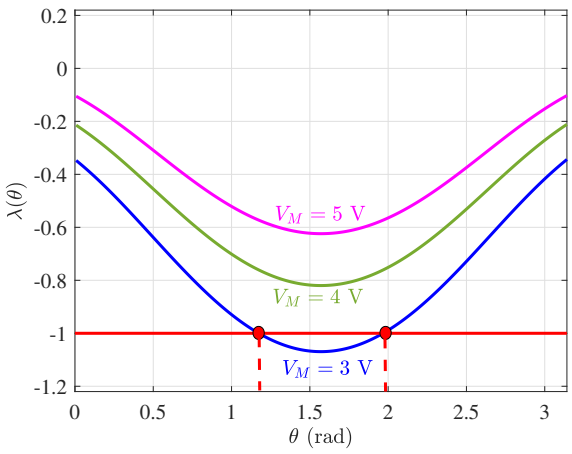

Figure 10. The eigenvalue $\lambda(\theta)$ as the phase angle is varied within $(0, \pi)$ for different values of V_M.

At the boundary of fast-scale instability, one has $\lambda_{\min} = -1$. By imposing this condition in (20), the following equation must hold

$$m_r = \frac{R_s m_0(\theta)}{2} \frac{1 - 2D(\theta)}{D(\theta)} \tag{21}$$

An upper bound of the left-hand side of (21) is $-R_s m_0(\theta)/2 = R_s v_{o1}(\theta)/(2L)$ which is obtained for $D = 1$ or equivalently for $\theta = \pi/2$. Therefore, the slope $m_r = R_s v_{o1}(\theta)/(2L)$ i.e., equal to one half the absolute value of the falling slope of the control signal σ will guarantee stability within the full range of $\theta \in (0, 2\pi)$. Therefore, to avoid the fast-scale instability for the full range of θ, an adaptive compensation scheme can be used where the amplitude of the compensating signal v_r is computed for each switching cycle according to the sampled voltage $v_{o1}(nT)$, $n \in \mathbb{N}$, the inductance value L and sensing resistance R_s. Therefore, the cycle-by-cycle adapted slope $m_r(nT)$ and amplitude $V_M(nT)$, $n \in \mathbb{N}$, of the compensating ramp signal v_r to guarantee a system free from fast-scale instability are

$$m_r(nT) = R_s \frac{v_{o1}(nT)}{2L} \qquad \text{and} \qquad V_M(nT) = R_s T \frac{v_{o1}(nT)}{2L} \tag{22}$$

The expression of the eigenvalue $\lambda(\theta)$ given in (20) is plotted in Figure 11 in terms of the phase angle θ with an adaptive slope compensation as given in (22). It can be observed that the eigenvalue $\lambda(\theta)$ fulfills the condition $-1 < \lambda(\theta) < 0$ for all values of phase angle $\theta \in (0, 2\pi)$ implying stability for all this range θ.

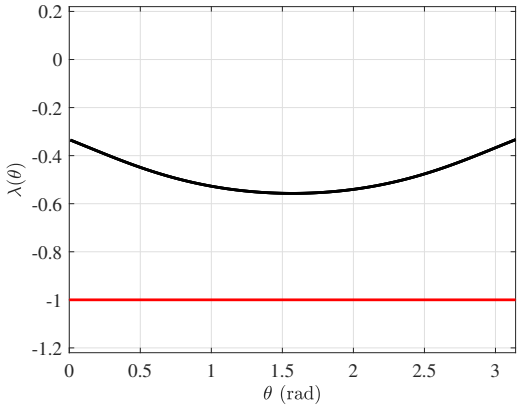

Figure 11. The eigenvalue $\lambda(\theta)$ as the phase angle is varied within $(0, \pi)$ with an adaptive compensation scheme using $m_r = -R_s m_0/2$.

4.3. Adaptive Slope Compensation Circuit

To generate an adaptive slope and amplitude according to (22), a circuit with an output signal v_r with the following expression must be used

$$v_r(t) = \frac{\kappa_r}{\tau_r} \int_0^{t \bmod T} v_{o1}(nT) \mathrm{d}\zeta \tag{23}$$

The integral is reset to zero at the beginning of each switching cycle of time period T. τ_r is the time constant of the resettable integrator and κ_r is a suitable gain to be selected in such a way that $\kappa_r/\tau_r = R_s/(2L)$. Since the switching ripple of the voltage v_{o1} is negligible, the instantaneous value $v_{o1}(t)$ of this voltage can be used in (23) instead of its sampled value $v_{o1}(nT)$ without significantly altering the results. With this slight modification, the new expression of the adaptive compensation signal becomes as follows

$$v_r(t) = \frac{\kappa_r}{\tau_r} \int_0^{t \bmod T} v_{o1}(\zeta) \mathrm{d}\zeta \tag{24}$$

The generation of the adaptive slope compensating signal can be performed by the circuit depicted in Figure 12. Without loss of generality, the resistance R_r and the capacitance C_r can be selected in such a way that $R_rC_r = 2L/R_s$ and the resistances R_1 and R_2 can be selected in such a way that $R_1/R_2 = \kappa_r$.

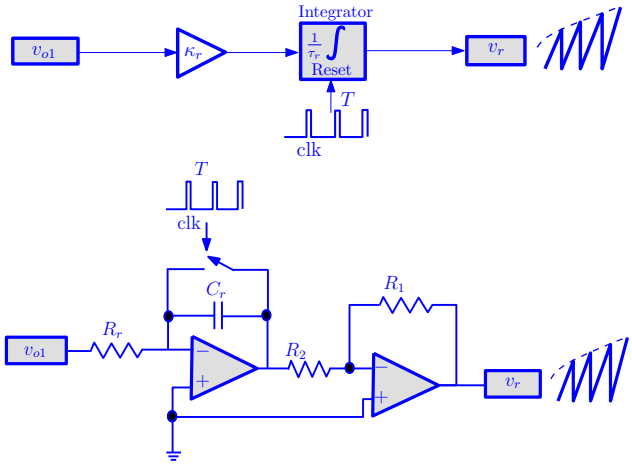

Figure 12. The block diagram (**top**) and the equivalent schematic circuit representation (**bottom**) of the adaptive compensating slope signal generator.

With the previous adaptive compensation scheme, a stable response for the system will be obtained regardless of the weather conditions. Figure 13 shows the duty cycle signal obtained from numerical simulations corresponding to the results presented in Figures 5–7 but with the compensating signal amplitude selected according to (24) using the circuit diagram of Figure 12 with $R_rC_r = 2L/R_s = 2$ ms ($C_r = 10$ nF and $R_r = 200$ kΩ) and $R_1 = R_2 = 10$ kΩ. For the sake of clarity only some switching cycles are represented in Figure 13. Notice that the fast-scale instability is completely suppressed and that the slope of the compensating signal is equal to one half the absolute value of the down slope of the signal σ for all the switching periods within the grid cycle hence guaranteeing stability for all values of the duty cycle D and phase angle θ.

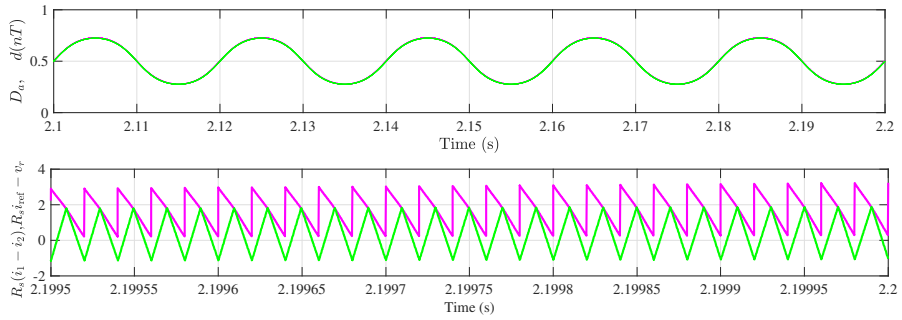

Figure 13. The time varying duty cycle calculated from (12) ($D(t)$) obtained from numerical simulation ($d(nT)$, $n \in \mathbb{N}$) for guaranteeing stability within the complete duty cycle range.

It is worth noting that for the parameter values considered in this study, the maximum value reached by the duty cycle is $D_{\max} \approx 0.72$ for $S = 200$ W/m^2. Therefore, the previous expression of the ramp signal can be multiplied by $D_{\max}$ and fast-scale instability will still be avoided.

Another choice of the slope of the compensating signal is by making it equal to the absolute value of the down slope of the signal σ, i.e., $m_r = R_s v_{o1}(\theta)/L$. This choice of the slope m_r of the compensating signal v_r not only guaranties fast-scale stability for all values of the duty cycle but also gives rise to a fastest or *deadbeat* response at the switching time scale [27]. The slope and amplitude guaranteeing this response are given by the following

expressions Another choice of the slope of the compensating signal is by making it equal to the absolute value of the down slope of the sensed signal σ, i.e., $m_r = R_s v_{o1}(\theta)/L$. This choice of the slope m_r of the compensating signal v_r not only guaranties stability for all values of the duty cycle but gives rise to a fastest or *deadbeat* response at the switching time scale [27]. The slope $m_r(nT)$ and amplitude $V_M(nT)$ guaranteeing this response are given by the following expressions

$$m_r(nT) = R_s \frac{v_{o1}(nT)}{L} \qquad \text{and} \qquad V_M(nT) = R_s T \frac{v_{o1}(nT)}{L}, \tag{25}$$

Figure 14 shows the waveforms of the quasi-steady-state duty cycle with the same parameter values used in Figure 13 but with the compensating signal slope and amplitude selected according to (25). From this figure, it can be observed that only the fast-scale instability is suppressed but the slope of the compensating signal is equal to the absolute value of the down slope of the sensed current σ hence guaranteeing a *deadbeat* response at the fast-scale within the full grid cycle. It is worth noting that the same circuit diagram of Figure 12 was used for obtaining the results depicted in Figure 14 but by selecting $R_r C_r = L/R_s = 1$ ms ($C_r = 10$ nF and $R_r = 100$ kΩ). With the previous adaptive compensation scheme, a *deadbeat* response for the system at the switching scale is obtained regardless of the weather conditions.

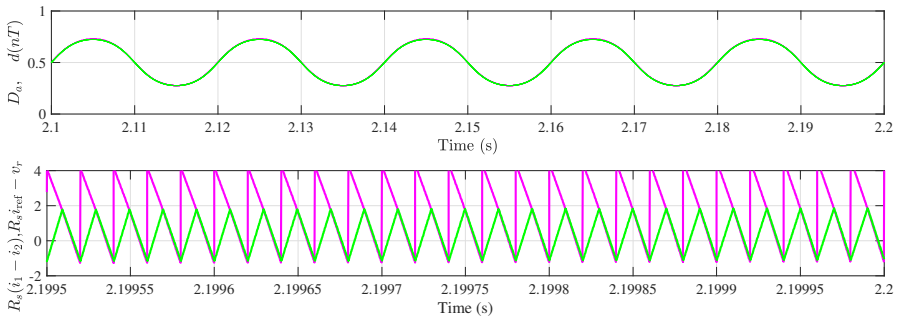

Figure 14. The time varying duty cycle calculated from (12) ($D(t)$) obtained from numerical simulation ($d(nT)$, $n \in \mathbb{N}$) for guaranteeing a *deadbeat* response within the complete duty cycle range.

5. Conclusions

The differential boost inverter is an interesting inverter topology providing a transformerless voltage step-up capability suitable for DC-AC modules in PV systems. This paper dealt with the nonlinear behavior and slope compensation of a grid-tied boost inverter under a differential peak current mode control for its operation as an AC module in a PV system. The module performs maximum power point tracking, DC PV voltage regulation and grid synchronization. A three-loop differential peak current mode-controlled PV-fed grid-tied boost inverter has been studied and its slope compensation has been addressed. The paper began with presenting detailed simulations that has shown that the system can exhibit fast-scale instability. This fact has been verified using numerical simulations from the switched model of the inverter for different irradiance levels. Accurate closed-form design-oriented expressions to predict fast-scale instability have been derived in terms of the system parameters and adaptive slope compensation schemes have been proposed to suppress the observed instability. The effectiveness of the proposed schemes has been confirmed by detailed numerical simulation performed on the circuit-level switched model. The results demonstrate the viability of differential peak current mode control with the proposed adaptive slope compensation for differential boost inverters that can be used as AC modules in PV systems.

Author Contributions: These authors contributed equally to this work. All authors have read and agreed to the published version of the manuscript.

Funding: The authors would like to acknowledge the support by the Spanish Ministerio de Economia y Competitividad under grants DPI2017-84572-C2-1-R. A.E.A. and M.A.-N. acknowledge financial support from the Researchers Supporting Project number (RSP-2020/150), King Saud University, Riyadh, Saudi Arabia.

Institutional Review Board Statement: Not aplicable.

Informed Consent Statement: Not aplicable.

Data Availability Statement: Not aplicable.

Conflicts of Interest: The authors delcare no conflict of interest.

References

1. Tse, C.K.; Huang, M.; Zhang, X.; Liu, D.; Li, X.L. Circuits and Systems Issues in Power Electronics Penetrated Power Grid. *IEEE Open J. Circuits Syst.* **2020**, *1*, 140–156. [CrossRef]
2. Romero-Cadaval, E.; Spagnuolo, G.; Franquelo, L.G.; Ramos-Paja, C.A.; Suntio, T.; Xiao, W.M. Grid-Connected Photovoltaic Generation Plants: Components and Operation. *IEEE Ind. Electron. Mag.* **2013**, *7*, 6–20. [CrossRef]
3. Meneses, D.; Blaabjerg, F.; García, O.; Cobos, J.A. Review and Comparison of Step-Up Transformerless Topologies for Photovoltaic AC-Module Application. *IEEE Trans. Power Electron.* **2013**, *28*, 2649–2663. [CrossRef]
4. Kouro, S.; Leon, J.I.; Vinnikov, D.; Franquelo, L.G. Grid-Connected Photovoltaic Systems: An Overview of Recent Research and Emerging PV Converter Technology. *IEEE Ind. Electron. Mag.* **2015**, *9*, 47–61. [CrossRef]
5. Sivasubramanian, P.T.; Mazumder, S.K.; Soni, H.; Gupta, A.; Kumar, N. A DC/DC Modular Current-Source Differential-Mode Inverter. *IEEE J. Emerg. Sel. Top. Power Electron.* **2016**, *4*, 489–503. [CrossRef]
6. Caceres, R.O.; Barbi, I. A boost DC-AC converter: Analysis, design, and experimentation. *IEEE Trans. Power Electron.* **1999**, *14*, 134–141. [CrossRef]
7. Lopez-Caiza, D.; Flores-Bahamonde, F.; Kouro, S.; Santana, V.; Müller, N.; Chub, A. Sliding Mode Based Control of Dual Boost Inverter for Grid Connection. *Energies* **2019**, *12*, 4241. [CrossRef]
8. Zhu, G.; Tan, S.; Chen, Y.; Tse, C.K. Mitigation of Low-Frequency Current Ripple in Fuel-Cell Inverter Systems Through Waveform Control. *IEEE Trans. Power Electron.* **2013**, *28*, 779–792. [CrossRef]
9. Flores-Bahamonde, F.; Valderrama-Blavi, H.; Bosque-Moncusi, J.M.; García, G.; Martínez-Salamero, L. Using the sliding-mode control approach for analysis and design of the boost inverter. *IET Power Electron.* **2016**, *9*, 1625–1634. [CrossRef]
10. El Aroudi, A.; Haroun, R.; Al-Numay, M.; Huang, M. Multiple-loop control design for a single-stage PV-fed grid-tied differential boost inverter. *Appl. Sci.* **2020**, *10*, 4808. [CrossRef]
11. Lopez, D.; Flores-Bahamonde, F.; Kouro, S.; Perez, M.A.; Llor, A.; Martínez-Salamero, L. Predictive control of a single-stage boost DC-AC photovoltaic microinverter. In Proceedings of the 42nd Annual Conference of the IEEE Industrial Electronics Society, Florence, Italy, 23–26 October 2016; pp. 6746–6751.
12. Leine, R.L.; Nijemeijer, H. Dynamics and bifurcations of non-smooth mechanical systems. In *Lecture Notes in Applied and Computational Mechanics*; Springer: Berlin/Heidelberg, Germany, 2004; Volume 18.
13. Huang, M.; Ji, H.; Sun, J.; Wei, L.; Zha, X. Bifurcation-Based Stability Analysis of Photovoltaic-Battery Hybrid Power System. *IEEE J. Emerg. Sel. Top. Power Electron.* **2017**, *5*, 1055–1067. [CrossRef]
14. Cheng, L.; Ki, W.; Yang, F.; Mok, P.K.T.; Jing, X. Predicting Subharmonic Oscillation of Voltage-Mode Switching Converters Using a Circuit-Oriented Geometrical Approach. *IEEE Trans. Circuits Syst. Regul. Pap.* **2017**, *64*, 717–730. [CrossRef]
15. Tse, C.K. *Complex Behavior of Switching Power Converters*; CRC Press: New York, NY, USA, 2003.
16. Mazumder, S.K; Nayfeh, A.H.; Borojevi, D. Theoretical and experimental investigation of the fast- and slow-scale instabilities of a DC-DC converter. *IEEE Trans. Power Electron.* **2001**, *16*, 201–216. [CrossRef]
17. Giaouris, D.; Banerjee, S.; Zahawi, B.; Pickert, V. Stability Analysis of the Continuous-Conduction-Mode Buck Converter via Filippov's Method. *IEEE Trans. Circuits Syst. I Regul. Pap.* **2008**, *55*, 1084–1096. [CrossRef]
18. Mandal, K.; Banerjee, S. Synchronization Phenomena in Microgrids With Capacitive Coupling. *IEEE J. Emerg. Sel. Top. Circuits Syst.* **2015**, *5*, 364–371. [CrossRef]
19. M. Huang, M.; Peng, Y.; Tse, C.K.; Liu, Y.; Sun, J.; Zha, X. Bifurcation and Large-Signal Stability Analysis of Three-Phase Voltage Source Converter Under Grid Voltage Dips. *IEEE Trans. Power Electron.* **2017**, *32*, 8868–8879. [CrossRef]
20. Robert, B.; Robert, C. Border Collision Bifurcations in a One-Dimensional Piecewise Smooth Map for a PWM Current-Programmed H-Bridge Inverter. *Int. J. Control.* **2002**, *7*, 1356–1367. [CrossRef]
21. Asahara, H.; Kousaka, T. Bifurcation analysis in a PWM current controlled H-bridge inverter. *Int. J. Bifurc. Chaos* **2011**, *21*, 985–996. [CrossRef]
22. Li, M.; Dai, D.; Ma, X. Slow-scale and fast-scale instabilities in voltage-mode controlled full-bridge inverter. *Circuits Syst. Signal Process.* **2008**, *27*, 811–831. [CrossRef]

23. Avrutin, V.; Morcillo, J.D.; Zhusubaliyev, Z.T.; Angulo, F. Bubbling in a power electronic inverter: Onset, development and detection. *Chaos Solitons Fractals* **2017**, *104*, 135–152. [CrossRef]
24. Lei, B.; Xiao, G.; Wu, X.; Ka, Y.R.; Zheng, L. Bifurcation analysis in a digitally controlled H-bridge grid-connected inverter. *Int. J. Bifurc. Chaos* **2014**, *24*, 1–15. [CrossRef]
25. Iu, H.H.C.; Zhou, Y.; Tse, C.K. Fast-scale instability in a boost PFC converter under average current control. *Int. J. Circuit Theory Appl.* **2003**, *31*, 611–624. [CrossRef]
26. El Aroudi, A.; Al-Numay, M.S.; Lu, W.G.; Bosque-Moncusi, J.M.; Iu, H.H. A Combined Analytical-Numerical Methodology for Predicting Subharmonic Oscillation in H-Bridge Inverters Under Double Edge Modulation. *IEEE Trans. Circuits Syst. Regul. Pap.* **2018**, *65*, 2341–2351. [CrossRef]
27. Erickson, R.W.; Maksimovic, D. *Fundamentals of Power Electronics*; Springer: Berlin/Heidelberg, Germany, 2001.
28. Mattingly, D. *Designing Stable Compensation Networks for Single Phase Voltage Mode Buck Regulators, Technical Brief*; Intersil: Milpitas, CA, USA, 2003.
29. The Ultimate Simulation Environment for Power Conversion and Motor Control. Available online: https://powersimtech.com/products/psim/ (accessed on 11 February 2021).
30. The Tallmax Plus Module. Available online: http://static.trinasolar.com/sites/default/files/US-Datasheet-DD14A(II).pdf (accessed on 11 February 2021).
31. El Aroudi, A.; Rodriguez, E.; Orabi, M.; Alarcon, E. Modeling of switching frequency instabilities in buck-based DC-AC H-bridge inverters. *Int. J. Circuit Theory Appl.* **2011**, *39*, 175–193. [CrossRef]
32. El Aroudi, A.; Orabi, M.; Martínez-Salamero, L. A representative discrete-time model for uncovering slow and fast scale instabilities in boost power factor correction AC-DC pre-regulators. *Int. J. Bifurc. Chaos* **2008**, *18*, 3073–3092. [CrossRef]
33. El Aroudi, A. A New Approach for Accurate Prediction of Subharmonic Oscillation in Switching Regulators: Part I: Mathematical Derivations. *IEEE Trans. Power Electron.* **2017**, *32*, 5651–5665. [CrossRef]
34. Ridley, R. A new, continuous-time model for current-mode control power convertors. *IEEE Trans. Power Electron.* **1991**, *6*, 271–280. [CrossRef]
35. El Aroudi, A.; Haroun, R.; Al-Numay, M.; Huang, M. Analysis of Subharmonic Oscillation and Slope Compensation for a Differential Boost Inverter. *Appl. Sci.* **2020**, *10*, 5626. [CrossRef]